Multiple Orientations in a Physiological Complex: The Pyruvate-Ferredoxin Oxidoreductase−Ferredoxin System‡

Laetitia Pieulle,§ Matthieu Nouailler,§ Xavier Morelli,§ Christine Cavazza,§,|| Philippe Gallice,⊥ Stéphane Blanchet,§ Pierre Bianco,§ Françoise Guerlesquin,§ and E. Claude Hatchikian*,§

Unité de Bioénergétique et Ingéniérie des Protéines, Institut de Biologie Structurale et Microbiologie, CNRS, 31 Chemin Joseph-Aiguier, 13402 Marseille Cedex 20, France, and Faculté de Pharmacie, Laboratoire de Prévention des Risques et Nuisances Technologiques-EA 1784, 27 bd. Jean Moulin, 13385 Marseille Cedex 05, France

Received July 5, 2004; Revised Manuscript Received September 28, 2004

ABSTRACT: Ferredoxin I from *Desulfovibrio africanus* (*Da* FdI) is a small acidic [4Fe-4S] cluster protein that exchanges electrons with pyruvate-ferredoxin oxidoreductase (PFOR), a key enzyme in the energy metabolism of anaerobes. The thermodynamic properties and the electron transfer between PFOR and either native or mutated FdI have been investigated by microcalorimetry and steady-state kinetics, respectively. The association constant of the PFOR−FdI complex is 3.85×10^5 M^{-1}, and the binding affinity has been found to be highly sensitive to ionic strength, suggesting the involvement of electrostatic forces in formation of the complex. Surprisingly, the punctual or combined neutralizations of carboxylate residues surrounding the [4Fe-4S] cluster slightly affect the PFOR−FdI interaction. Furthermore, hydrophobic residues around the cluster do not seem to be crucial for the PFOR−FdI system activity; however, some of them play an important role in the stability of the FeS cluster. NMR restrained docking associated with site-directed mutagenesis studies suggested the presence of various interacting sites on *Da* FdI. The modification of additional acidic residues at the interacting interface, generating a FdI pentamutant, evidenced at least two distinct FdI binding sites facing the distal [4Fe-4S] cluster of the PFOR. We also used a set of various small acidic partners to investigate the specificity of PFOR toward redox partners. The remarkable flexibility of the PFOR−FdI system supports the idea that the specificity of the physiological complex has probably been "sacrificed" to improve the turnover rate and thus the efficiency of bacterial electron transfer.

Oxidative decarboxylation of pyruvate to form acetyl-coenzyme A is a crucial step in cell metabolism. In aerobic organisms, this reaction is catalyzed by the pyruvate dehydrogenase multienzyme complex (PDH).[1] In most anaerobic bacteria, the reaction is carried out by the pyruvate-ferredoxin oxidoreductase (PFOR). The electron acceptor of this single enzyme is either a [4Fe-4S] ferredoxin or a flavodoxin. Although both PFOR and PDH are thiamin pyrophosphate (TPP)-containing enzymes, only the former can carry out the reverse reaction, that is, the reductive carboxylation of acetyl-CoA to yield pyruvate. This reaction constitutes the basis for CO_2 fixation in green photosynthetic and acetogenic bacteria (*1*) and in methanogens (*2*). PFORs are homodimeric, heterodimeric, or heterotetrameric enzymes that are phylogenetically related.

The structure of *Desulfovibrio africanus* (*Da*) PFOR has been determined by X-ray crystallography (*3*). This homodimeric enzyme contains one TPP molecule per subunit, buried in the protein, and three $[4Fe\text{-}4S]^{2+/1+}$ clusters with midpoint potentials ranging from −540 to −390 mV (*4*). These redox centers are regularly disposed between the active site and the molecular surface, providing a potential electron transfer pathway (*5*). In *Da*, three ferredoxins (Fds) have been isolated and characterized (*6*); the monocluster ferredoxin I (FdI), the most abundant, is a small protein (7.5 kDa) containing one $[4Fe\text{-}4S]^{2+/1+}$ cluster with a low redox potential ($E^{o\prime} = -385$ mV), and its structure has been determined by both X-ray crystallography (*7*) and NMR (*8*). Kinetic parameters of the electron transfer between PFOR and FdI from *Da* have been previously determined by electrochemistry (*6*). The second-order rate constant is 7×10^7 M^{-1} s^{-1}, and the K_m value of the enzyme for FdI is 3 μM. The fast electron transfer between *Da* PFOR and FdI suggests that a transient complex is formed. Cross-linking experiments between PFOR and FdI have shown that the

‡ Nucleotide sequence data are available in the DDBJ, EMBL, and GenBank databases under accession number AJ489482.

* To whom correspondence should be addressed: Unité de Bioénergétique et Ingéniérie des Protéines, IBSM, CNRS, 31, Chemin Joseph-Aiguier, 13402 Marseille Cedex 20, France. Telephone: 33 4 91 16 41 45. Fax: 33 4 91 16 45 78. E-mail: hatch@ibsm.cnrs-mrs.fr.

§ CNRS.

|| Present address: Laboratoire de Cristallographie et Cristallogenèse des Protéines, Institut de Biologie Structurale Jean-Pierre Ebel, Commissariat à l'Energie Atomique, Université Joseph Fourier, CNRS, 41, Jules Horowitz, 38027 Grenoble Cedex 1, France.

⊥ Laboratoire de Prévention des Risques et Nuisances Technologiques-EA 1784.

[1] Abbreviations: PFOR, pyruvate-ferredoxin oxidoreductase; PDH, pyruvate dehydrogenase multienzyme complex; TPP, thiamin pyrophosphate; *Da*, *Desulfovibrio africanus*; Fds, ferredoxins; *Dg*, *Desulfovibrio gigas*; *Tc*, *Thermodesulfobacterium commune*; *Dmn*, *Desulfomicrobium norvegicum*; *Cp*, *Clostridium pasteurianum*; *S*sp., *Spirulina* sp.; FdI, ferredoxin I; FdII, ferredoxin II; htFdI, His-tagged ferredoxin I; IPTG, isopropyl β-D-thiogalactopyranoside; DTE, dithioerythritol; ITC, isothermal titration calorimetry; PCR, polymerase chain reaction; HSQC, heteronuclear single-quantum correlation.

10.1021/bi0485878 CCC: $27.50
Published on Web 11/17/2004

Table 1: Template and Oligonucleotide Primer DNA Sequence

mutant	template	oligonucleotide[a]
E15A	pLF1	(+200stop+cattgcctgcg**CG**tcctgcgtggagatcgcacc)+(−200pTac+cacgcagga**CG**cgcaggcaatgcattcg)
D7A/D9A/E10A	pLF1	taggtacccaaggaggcatcaatg(cac)$_6$gctcgcaagttctatgta**GCG**cag**GCGGCG**tgcattgcc+FdI*Bam*HI[b]
Δ62−64	pLF1	ttggatccgcctaccaatggatgctctgcacagg+FdI*Kpn*I[b]
D7A/D9A/E10A/ Δ62−64	pLF1var.$_{D7A/D9A/E10A}$	ttggatccgcctaccaatggatgctctgcacagg+FdI*Kpn*I[b]
D7A/D9A/E10A/ D28N/E30Q/E32Q	pLF1var.$_{D7A/D9A/E10A}$	(+200stop+tgccatg**A**acccg**C**agatt**C**agaaggcctatgtc)+(−200pTac+ggccttct**G**aatct**G**cgggt**T**-catggcaaaggcg)
D52R	pLF1	(+200stop+gtcgaggaggccatg**CG**tacctgccctgtg)+(−200pTac+cacagggcaggta**CG**catggcctcctcgac)
D52A/E48A/E49A	pLF1	(+200stop+ccaggaagaagtcg**CT**g**C**ggccatgg**CA**acctgccctgtg)+(−200pTac+cacagggcaggt**TG**-ccatggcc**G**c**AG**cgacttcttcctgg)
D52A/ E45A/E46A/ E48A/E49A	pLP1	(+200stop+gcgccagccagg**CT**g**C**agtcg**CT**g**C**ggccatgg**CA**acctgccctgtg)+(−200pTac+cacagg-gcaggt**TG**ccatggcc**G**c**AG**cgact**G**c**AG**cctggctggcgc)
I12T	pLF1	taggtacccaaggaggcatcaatg(cac)$_6$gctcgcaagttctatgtagaccaggacgaatgc**ACC**gcctgcg+FdI*Bam*HI[b]
I12E	pLF1	taggtacccaaggaggcatcaatg(cac)$_6$gctcgcaagttctatgtagaccaggacgaatgc**GAA**gcctgcg+FdI*Bam*HI[b]
I20E	pLF1	(+200stop+tcctgcgtggag**GAA**gcaccgggcgcc)+(−200pTac+ccggtgc**TTC**ctccacgcaggattcgc)
Y35E	pLF1	(+200stop+gattgagaaggcc**GAA**gtcaaggacgtg)+(−200pTac+cgtccttgac**TTC**ggccttctcaatctcc)
M27E	pLF1	(+200stop+gcctttgcc**GAA**gacccggagattgagaagg)+(−200pTac+ctccgggtc**TTCg**gcaaaggcgcc)

[a] Change made to the native sequence at the position indicated in bold capital letters. [b] Described in Experimental Procedures: +200 stop primer, 5′-gcgtttcacttctgagttcgg-3′; −200 pTac primer, 5′-gcagaaacgtggctggcctgg-3′. The mutagenic oligonucleotides are written in the usual 5′−3′ direction.

covalent complex exhibits a stoichiometry of one FdI for one PFOR monomer (*6*). The formation of the cross-linked complex and the electron transfer between the two redox partners are sensitive to the ionic strength, suggesting that electrostatic interactions are the driving force in formation of the complex (*6*). The molecular surface in the vicinity of the distal $[4Fe\text{-}4S]^{2+/1+}$ cluster of PFOR displays several positively charged conserved residues that constitute a potential recognition site for the negatively charged surface of FdI (*3*).

Electron transfer between proteins generally requires formation of a transient complex that brings together the two redox centers exchanging electrons to achieve a high turnover rate. It is generally assumed that the formation of the complex takes place in two stages, including (i) the initial encounter dominated by relatively long-range electrostatic forces and (ii) the second state involving additional short-range forces that include hydrogen bonds, van der Waals forces, and hydrophobic interactions; these make important contributions both to the overall binding energy and to the specificity of the interaction (*9*). This study was designed to extend our knowledge of the structural features that are involved in the binding and subsequent electron transfer between PFOR and FdI. The cocrystallization of the PFOR−FdI complex is a real challenge; an alternative to obtaining a structural model of the complex is NMR-restrained docking (*10*) associated with site-directed mutagenesis data.

With this aim in mind, the cDNA encoding *Da* FdI was cloned and sequenced and the recombinant FdI was expressed in *Escherichia coli*. In an effort to evaluate the role of electrostatic forces in formation of the complex, most of the FdI negatively charged surface residues (15 of 18) were then substituted with either a neutral or a charge-reverse residue or deleted. Therefore, a panel of FdI molecular variants, including one, three, five, or six carboxylate residues replaced simultaneously, was generated. Thermodynamic parameters of formation of the complex were analyzed through microcalorimetry experiments, and the electron transfer efficiency was characterized by steady-state kinetics. NMR-restrained docking was used to clarify the effects induced by carboxylate residue substitutions and suggested a new set of mutations.

EXPERIMENTAL PROCEDURES

Bacterial Strain

E. coli strain TG1 [*supE hsd*Δ*5 thi*Δ*(lac-proAB)* F′[*traD36 proAB*$^+$ *lacI*^{q} *lacZ*] Δ*M15*] was used for *Da* FdI expression.

Cloning and Sequencing of the fd1 Gene

Cloning of the *fd1* gene was carried out as previously described (*11*). The degenerate oligonucleotides [5′-TAY GTN GAY CAR GAY GAR TG-3′] and [5′-TCR TCY TCC CAR TGD ATR CA-3′] were derived from the amino acid sequence of *Da* FdI (*7*). The PCR product was cloned directly into the pCR2.1 vector using the TA cloning kit (Invitrogen) and sequenced. Two outward-facing oligonucleotides, [5′-CTT CTC AAT CTC CGG GTC CAT GGC-3′] for the 5′-extremity of the *fd1* gene and [5′-AGC CAG GAA GAA GTC GAG GAG GCC-3′] for the 3′-extremity of the *fd1* gene, were used for inverse PCR.

Site-Directed Mutagenesis of Da FdI

The *fd1* gene was amplified by PCR using oligonucleotides FdI*Kpn*I and FdI*Bam*HI as primers. The sequence of FdI*Kpn*I [5′-TAG GTA CCC A**AG GAG G**CA TCA **ATG (CAC)$_6$** GCT CGC-3′] is composed of a *Kpn*I recognition site (underlined in the sequence) followed by the putative ribosome binding site of the *fd1* gene (boldface in the sequence), and then 20 nucleotides corresponding to the beginning of the *fd1* coding sequence, including the ATG and six triplets (boldface) encoding the His-tagged domain for convenient purification. The sequence of FdI*Bam*HI [5′-T TGG ATC CGC **CTA** CTC GTC CTC CCA ATG GAT GC-3′] contains a *Bam*HI cleavage site (underlined) followed by two nucleotides, a triplet complementary to the stop codon (boldface), and nucleotides complementary to the 3′-end of the *fd1* coding sequence. The *Kpn*I−*Bam*HI fragment was introduced into the polylinker cloning site of plasmid pJF119EH (*11*) to give plasmid pLF1. FdI mutants were

prepared from plasmid pLF1 using a PCR-based procedure. Primers for mutagenesis are listed in Table 1. The *fd1* gene was sequenced to verify the mutations and to check for any mistakes that might have occurred elsewhere.

Expression and Purification of Da Recombinant FdI and Molecular Variants

Recombinant FdI and molecular variants were expressed in *E. coli*. Cells were grown aerobically at 37 °C in a modified Terrific Broth medium containing 12 g of yeast extract (Difco), 10 g of bacto-tryptone (Difco), 12.5 g of K_2HPO_4, 2.3 g of KH_2PO_4, 8 mL of glycerol, and 1000 mL of distilled water. Before inoculation, the medium was supplemented with 100 mg/L ferric ammonium citrate according to the method of ref *12* and 100 mg/L ampicillin. Large-scale cultures were grown in a 10 L fermentor (Chemap) while being stirred at 400 rpm with an aeration of 10 L/min. When the culture reached 1.3 A_{600} units, production of FdI was induced for 3 h with 0.5 mM IPTG (isopropyl β-D-thiogalactopyranoside), and the growth medium was supplemented once more with ferric ammonium citrate. The cells (180 g) were harvested by centrifugation at 50000*g* in a continuous-flow centrifuge (Sharples) when the growth reached 12 A_{600} units and stored at −80 °C. The harvested cells were resuspended with 20 mM potassium phosphate (pH 8.0) and 500 mM NaCl (buffer A) containing 1 μM deoxyribonuclease I (Sigma). The cells were passed once through a French pressure cell at 100 MPa, and cell debris was removed by centrifugation at 35000*g* for 20 min. All further purification steps were carried out under a nitrogen atmosphere. The supernatant was treated with deoxyribonuclease I and ribonuclease A (1 μM each, Sigma) at 30 °C for 30 min and subsequently centrifuged at 120000*g* for 90 min. The soluble protein fraction which contains *Da* His-tagged FdI (htFdI) was further purified by affinity chromatography on a Ni−NTA agarose (Qiagen) column. The soluble extract was loaded onto the column (2.6 cm × 1.5 cm) equilibrated with buffer A containing 5 mM imidazole. The column was washed first with 150 mL of the same buffer followed by 40 mL of buffer A containing 15 mM imidazole. Finally, the brown protein band bound at the top of the column was eluted with buffer A containing 80 mM imidazole. The htFdI-containing fraction was subsequently concentrated on a YM10 membrane (Centriplus, Amicon) and purified by gel filtration on a Sephacryl S-100 HR (Pharmacia) column (85 cm × 2.6 cm) equilibrated with 50 mM Tris-HCl buffer (pH 8.5). The Fd fraction was then concentrated on a YM10 membrane and stored in liquid nitrogen. At this stage, *Da* htFdI was considered to be pure on the basis of both polyacrylamide gel electrophoresis and absorption ratio ($A_{385}/A_{283} = 0.58$) (*13*).

^{15}N labeling of htFdI and the FdI pentamutant was carried out by growing *E. coli* cells in 4 L of minimal medium (M9) supplemented with [^{15}N]ammonium sulfate (1 g/L) and glucose as a carbon source (8 g/L). Cell growth conditions and protein expression were the same as described before, and ferric ammonium citrate was omitted.

Proteins and Enzyme Purification

PFOR, FdI, and ferredoxin II (FdII) were purified from *Da* (NCIMB 8401) as previously described (*4*, *13*). The purification procedures for cytochrome c_3, FdI and FdII, flavodoxin, and rubredoxin from *Desulfovibrio gigas* (*Dg*) (*14*) as well as *Thermodesulfobacterium commune* (*Tc*) Fd (*15*) were previously reported. *Desulfomicrobium norvegicum* (*Dmn*) FdI and FdII were purified as described previously (*16*). *Clostridium pasteurianum* (*Cp*) Fd and *Aquifex aeolicus* Fd 1 were gifts from J.-M. Moulis and J. Meyer, respectively (DBMS, CEA, Grenoble, France). *Spirulina* sp. (*S*sp.) Fd was purchased from Sigma.

Analytical Methods

Gel Electrophoresis. Slab gel electrophoresis in the presence of SDS was performed according to the method of Laemmli (*17*), with a 15% polyacrylamide running gel. Protein samples were previously heated at 100 °C for 5 min in the presence of 2% SDS and 1 mM mercaptoethanol. Protein bands were visualized by staining with Coomassie blue R250.

S-Carboxymethylation and Sequence Determination. htFdI was reduced and S-carboxymethylated as previously reported (*18*), and N-terminal amino acid sequence determination was performed by stepwise Edman degradation using a model 473A automatic sequencer (Applied Biosystems).

UV−Visible Spectroscopy. Absorption spectra were carried out on a model UV 1601 spectrophotometer (Shimadzu). The concentrations of *Da* PFOR and FdI as well as its molecular variants were determined using molecular extinction coefficients of 105 mM^{-1} cm^{-1} at 400 nm and 15 mM^{-1} cm^{-1} at 385 nm, respectively.

Activity Assay

The biological activity of htFdI and molecular variants was assessed in a coupled assay system in which FdI reduced by PFOR was subsequently reoxidized by an excess of cytochrome c_3. This assay allows us to maintain a constant amount of oxidized FdI in the reaction mixture. Previous data indicate that electron transfer from Fd to cytochrome c_3 (*19*) is faster than that from PFOR to Fd (*6*). *Dg* cytochrome c_3 was used in the coupled assay because direct reduction of this cytochrome by PFOR is negligible. Assays were performed under anaerobic conditions at 30 °C in rubber-stoppered cuvettes (total volume of 0.5 mL) containing 50 mM Tris-HCl buffer (pH 8.5), 10 mM pyruvate, 0.2 mM CoASH, 0.2−15 μM *Da* FdI, and 40 μM *Dg* cytochrome c_3. After the cuvette had been bubbled for 20 min with argon, PFOR (2−3 pmol) was injected and the reduction of cytochrome c_3 was monitored at 552 nm. Initial rates of cytochrome c_3 reduction were calculated using a difference absorption coefficient of 88 mM^{-1} cm^{-1} at 552 nm. Under our assay conditions, the oxidation of one molecule of pyruvate catalyzed by PFOR is coupled to the reduction of two molecules of *Da* FdI, whereas the reduction of one molecule of tetraheme cytochrome c_3 corresponds to the reoxidation of four molecules of FdI reduced by PFOR. The kinetic parameters have been adjusted to the hyperbola equation according to the Cleland method (*20*).

For evaluating the reactivity of *Da* PFOR toward various natural electron carriers, the activity of the enzyme has been determined by measuring the level of reduction of the electron acceptor at 420 nm for ferredoxins, 456 nm for flavodoxin, and 490 nm for rubredoxin. Assays were carried

out under anaerobic conditions in a serum-stoppered cuvette containing 50 mM Tris-HCl buffer (pH 8.5), 10 mM pyruvate, 0.2 mM CoASH, 20 μM electron carrier, and 16 mM DTE, in a final volume of 0.5 mL. The reaction was started by injection of PFOR (0.4 pmol).

Electrochemical Measurements

Cyclic (CV) and square-wave (SWV) voltammetry were carried out using an EG&G 273A potentiostat modulated by EG&G PARC M270/250 software. A three-electrode cell consisting of a Metrohm Ag |AgCl| saturated NaCl reference electrode (having a potential of 210 mV vs the normal hydrogen electrode), a gold wire auxiliary electrode, and a working pyrolytic graphite electrode was used throughout. Before each experiment, the working electrode was polished with 0.05 μM alumina slurry. Because of the excess of negative charges of acidic proteins such as htFdI or molecular variants, the rate of electron transfer to or from the working electrode required the concentration of the polycations added to the solution, here 10 μM poly(L-lysine), to be increased (*21*), and thus the electrode responses to be detected. The reversibility of electron exchanges was established from CV curves, and the redox potential values were calculated from SWV peak potentials. All experiments were performed at room temperature, in 0.01 M Tris-HCl (pH 7.6) under an argon atmosphere.

Isothermal Titration Calorimetry Analysis

Reagents. Da PFOR and FdI solutions were equilibrated in 10 mM Tris-HCl (pH 8.5) and 8.55 mM NaCl to obtain concentration values close to 10 μM and 3.7 mM, respectively. To obtain PFOR and FdI under identical buffering conditions, the protein solutions were extensively dialyzed and concentrated by ultrafiltration using Centricon-10 concentrators (10 000 MW cutoff, Amicon) for FdI and Centricon-50 concentrators (50 000 MW cutoff, Amicon) for PFOR.

Isothermal Titration Calorimetry (ITC). Equilibrium binding experiments designed to study the interaction between PFOR and FdI were performed at 298 K using a 2277 Thermal Activity Monitor calorimeter (Thermometric) equipped with a titration unit. Data acquisition and analyses were carried out using DIGITAM 4.1 (Thermometric). In a typical experiment, titration was performed as follows. Ten aliquots (5 μL each) of the FdI solution were injected from a 100 μL syringe into the calorimeter cell containing the PFOR solution (0.9 mL) to achieve a complete binding isotherm. The effective heat of binding was obtained by subtracting the heat of dilution (measured by additional injections of the FdI solution after saturation) from the heat of reaction. The binding enthalpy ($\Delta H°$) and affinity constant (K_a) were then obtained by fitting the experimentally corrected binding isotherm to a model incorporated into DIGITAM, assuming one set of binding sites. Changes in free energy ($\Delta G°$) and entropy ($\Delta S°$) are obtained by the calculation $\Delta G° = -RT \ln K_a = \Delta H° - T\Delta S°$.

According to the methodology described, ITC was used in a set of experiments to investigate the effect of ionic strength on the interaction. Titrations were thus carried out in 10 mM Tris-HCl (pH 8.5) with 0.015, 0.03, and 0.1 M NaCl.

NMR-Restrained Docking

NMR. NMR experiments were carried out on a Bruker DRX 500 spectrometer at 298 K. The assignments of ^{1}H and ^{15}N chemical shifts of htFdI and the pentamutant were obtained from three-dimensional NOESY-HSQC and HNHA experiments performed on a ^{15}N-labeled FdI sample at a concentration of 0.7 mM in 20 mM phosphate buffer (pH 6.1) and 10% D_2O. Proton chemical shifts were found to be in agreement with previous FdI homonuclear assignments (*8*).

NMR titrations were performed using two-dimensional HSQC experiments, recorded using a Watergate pulse sequence in the TPPI mode, on a 0.06 mM htFdI or pentamutant sample in the absence or presence of various molar equivalents of PFOR (0.1, 0.2, 0.5, and 1). In HSQC experiments, the chemical shift variations are observed on exposed NH groups located at the interacting site, the side chains of the corresponding residues being buried in the molecule (this is the case for hydrophobic residues such as Val or Ile). Residues involved in protein−protein interactions (like acidic residues) have exposed side chains and buried NH groups. The NH resonances of these residues may be not affected by formation of the complex. Thus, chemical shift variations give the mapping of an interacting site. The spectral widths are 2000 Hz for ^{1}H and 2027 Hz for ^{15}N; 1024 data points in t_2 and 64 transients for each of 128 t_1 points were used.

Docking. Ab initio docking calculations were performed using BiGGER version 1.0 (*22*). The algorithm starts with the atomic coordinates of the two proteins (PDB entry 1FXR for FdI and PDB entry 1B0P for PFOR). For the pentamutant, a model has been generated by residue substitutions in the FdI structure. Dockings were obtained after a systematic search of the binding space of both molecules (10° rotation, 1 Å translation), and the algorithm generates a population of 5000 hypothetical complexes. These solutions are ranked according to a scoring function which combines several interaction terms that are thought to be relevant for the stabilization of protein complexes: geometric packing of surfaces, electrostatic interactions, desolvation energy, and pairwise propensities of the amino acid side chains to make contact across the molecular interface.

NMR Filtering. Chemical shift variations induced by complex formation were used to select the best model obtained from *ab initio* calculation, according to the restrained docking approach (*23*). A combination of ^{1}H and ^{15}N chemical shift variations was used for NMR filtering. Chemical shift variations of >0.012 ppm are considered to be significant. The chemical shift variations were converted into distances (a nucleus is affected when it is within 5 Å of any atoms of the partner).

The representation of the protein structure was obtained using Pymol 0.95 from W. L. DeLano [*PyMOL* (2002) DeLano Scientific, San Carlos, CA].

RESULTS

Characterization of the PFOR−FdI Complex by ITC

The *Da* PFOR−FdI electron transfer complex has been characterized by electrochemistry (*6*). In the work presented here, we have established two sets of data, the thermodynamic parameters obtained from ITC and electron transfer

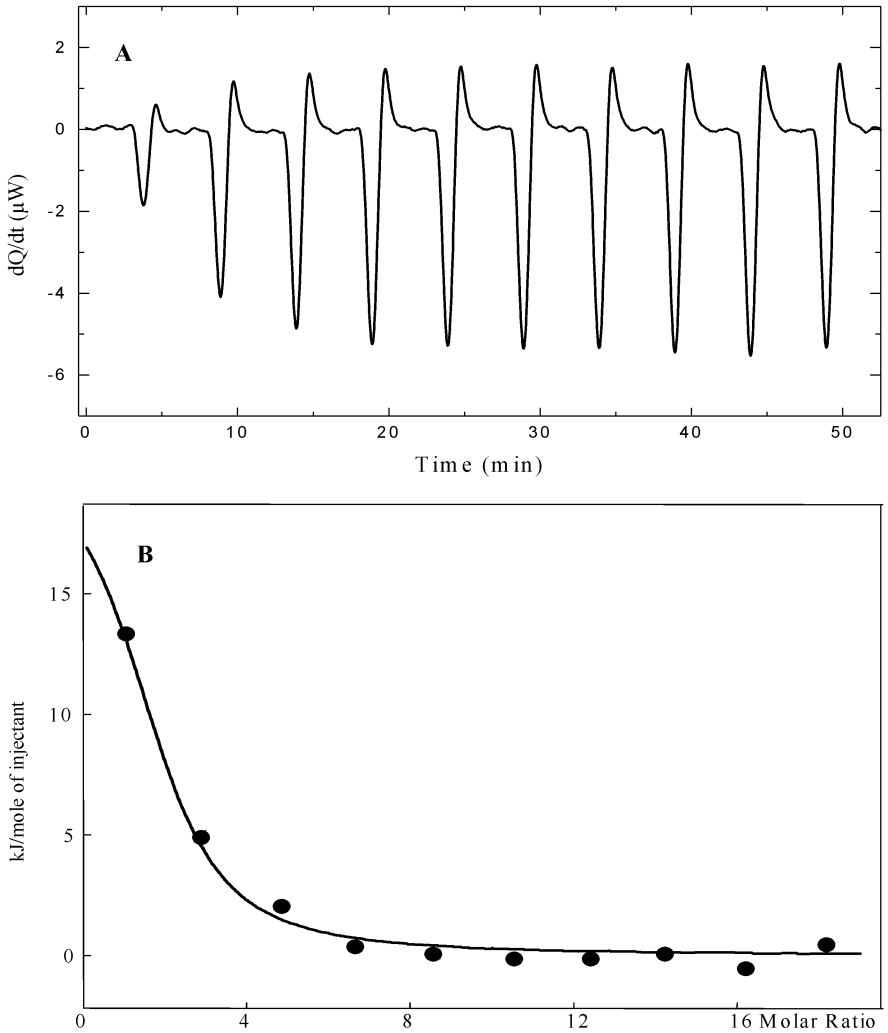

FIGURE 1: Heats of binding (A) and binding isotherm (B) for the calorimetric titration of 10.7 μM PFOR with 5 μL injections of 3.87 mM FdI (wild-type) in 10 mM Tris-HCl buffer and 8.55 mM NaCl at pH 8.5 and 298 K.

parameters obtained by steady-state kinetics using spectrophotometry.

Formation of the PFOR−FdI complex produces an endothermic heat of binding (Figure 1A). A typical calorimetric titration curve is obtained, indicating a stoichiometry of complex formation of two molecules of FdI per dimer of PFOR (Figure 1B). The association constant (K_a) determined from the plot is 3.85×10^5 M^{-1}. The enthalpy change ($\Delta H°$) is 21.3 kJ/mol, and the entropy change ($\Delta S°$) is 0.178 kJ mol^{-1} K^{-1}. These values indicate that hydrophobic interactions contribute to complex formation, but are also consistent with electrostatic interactions associated with the release of solvated water molecules. Consequently, it is difficult to identify the driving force for the interaction from thermodynamic data alone (*24*).

The electrostatic interactions were studied by altering the ionic strength of the buffer with NaCl. At a total ionic strength of 100 mM, the binding was too weak to be assessed. An increase in ionic strength from 10 to 30 mM weakens the binding of FdI by a factor 6.5, indicating that electrostatic interactions are essential in complex formation as already suggested by kinetics measurements (*6*). The increase in ionic strength induces a decrease in the entropic driving force (from 0.178 to 0.147 kJ mol^{-1} K^{-1}), whereas the enthalpy change becomes more favorable (from 21.3 to 16.5 kJ/mol).

Effects of FdI Substitutions on the PFOR−FdI Complex

Cloning, Expression, and Characterization of Da FdI. The gene encoding *Da* FdI was cloned and sequenced. The *fd1* gene nucleotide sequence was submitted to the EMBL/GenBank (accession number AJ489482) and found to be in agreement with the protein sequence previously reported (*7*). Moreover, the absence of an N-terminal signal peptide confirmed the presumed cytoplasmic localization of FdI. The *fd1* coding sequence was cloned downstream from the IPTG-inducible *tac* promoter of plasmid pJF119EH, and FdI was isolated using a histidine tag at the N-terminus. The purification procedure of htFdI yielded 1.6 mg of pure protein per liter of culture. Amino acid sequencing of the carboxymethylated htFdI showed the presence of a single polypeptide chain with the N-terminal sequence of *Da* FdI (ARKFYVDQDEC), preceded as expected by the six histidine residues. The redox potential, UV−visible, and EPR spectroscopic features of the htFdI (not shown) are indistinguishable from those of the wild type (*13*, *25*). Kinetic parameters of the reduction of FdI and htFdI were determined (K_m = 0.8 μM and k_{cat} = 139 s^{-1}). The K_m value for FdI measured in the coupled assay with cytochrome c_3 is 3−4-fold lower than the values previously obtained using the coupled assay with metronidazol or the electrochemical method (*6*).

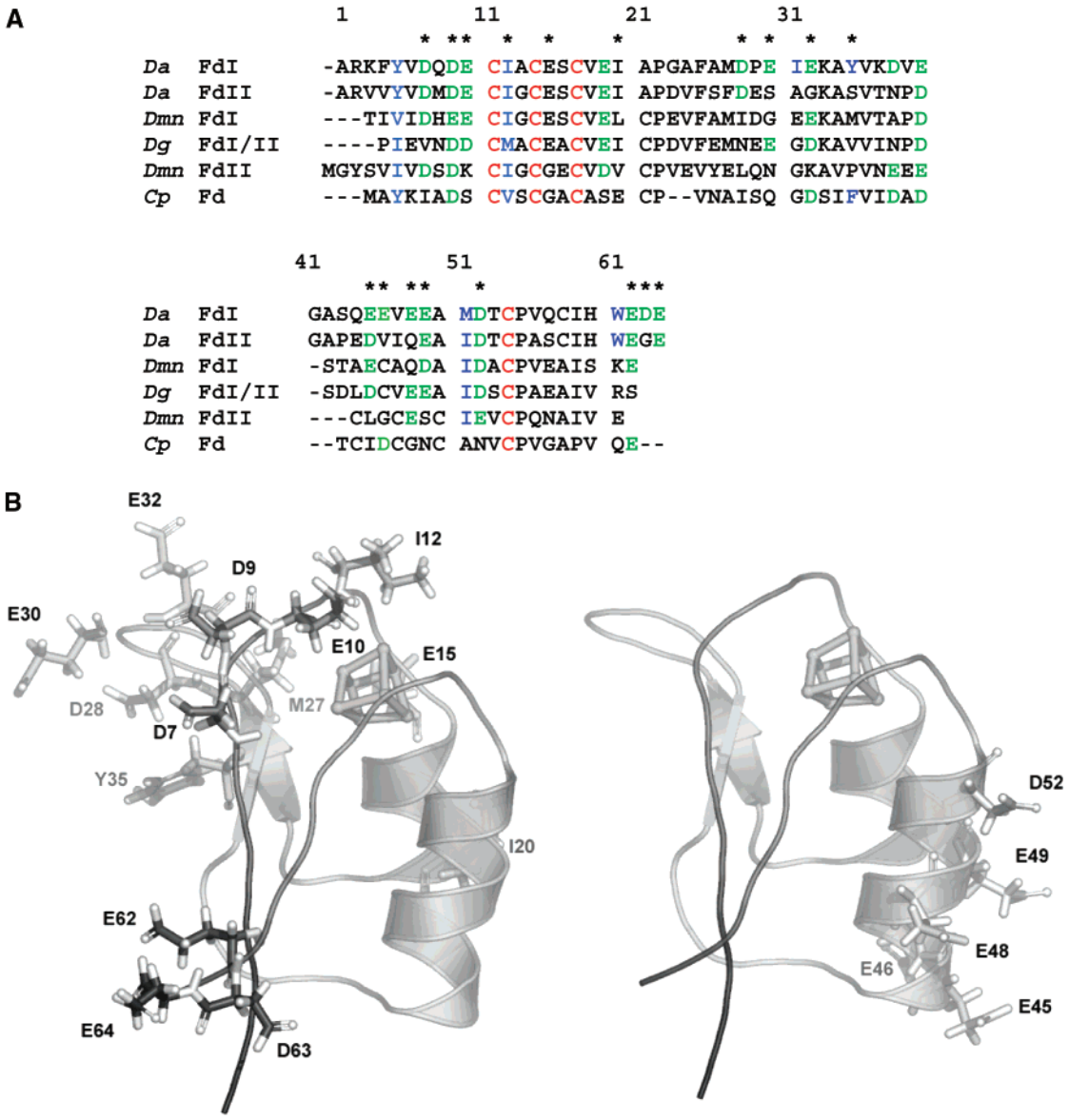

FIGURE 2: (A) Sequence alignment of Fds from *Da*, *Dmn*, *Dg*, and *Cp*. Sequences were aligned using Clustal W. The numbering corresponds to the *Da* FdI sequence. FeS ligand cysteines are colored red. Acidic residues at the interacting surface of FdI and conserved in other Fds are colored green. Hydrophobic residues at the interacting surface and conserved in other Fds are colored blue. Asterisks denote the mutated residues in *Da* FdI. (B) Structure of *Da* FdI (PDB entry 1FXR). On the left are represented the side chains of the first set of mutated residues (top part of Tables 2 and 3). On the right are represented the side chains of the second set of mutated residues suggested to be involved in formation of the complex by NMR experiments (bottom part of Tables 2 and 3).

Substitution of Charged Residues. Da FdI contains a great number of anionic residues (18 aspartic or glutamic acid of 64 residues) spread at the surface of the molecule (Figure 2B), and many of them are highly conserved in the sequences of *Desulfovibrio* monocluster ferredoxins (Figure 2A). Therefore, seven carboxylates (D7, D9, D28, E10, E15, E30, and E32) surrounding the [4Fe−4S] cluster were selected as primary targets for site-directed mutagenesis (Figure 2B). Many kinds of substitutions involving one, three, and up to six carboxylates at the same time have been performed (Table 2). Moreover, the C-terminal extremity (E62-D63-E64), which forms a highly negative hook pointing out of the FdI molecule proposed to play a role in the recognition of the redox partner (*6*), has been deleted (Figure 2B).

The expression of all the variants was similar to that of htFdI except for the D7A/D9A/E10A/D28N/E30Q/E32Q and D7A/D9A/E10A/Δ62−64 mutants which yielded only 30% of that of the recombinant protein. The values of the midpoint redox potentials of the variants indicate that neutralization of surface acidic residues by site-directed mutagenesis has no appreciable effect on the cluster redox potential (top part of Table 2). These results agree with those previously obtained with *Azotobacter vinelandii* FdI (*26*).

The kinetic parameters of the reduction of *Da* FdI variants by PFOR were compared to those of FdI (top part of Table 2). None of the variants for which one or several carboxylic groups were substituted displayed a change in V_{max}/K_m larger than 20% of the ratio exhibited by FdI. Moreover, the highly acidic C-terminal extremity of the FdI molecule seems not to be critical for the interaction with PFOR.

Calorimetric titration was performed for five variants (Table 3). The instability of the D7A/D9A/E10A/Δ62−64 variant has not allowed a precise determination of its K_a. htFdI and the E15A variant exhibit K_a values similar to that

Table 2: Comparison of Redox Potentials (±10 mV) and Kinetic Parameters of *Da* Recombinant FdI and Molecular Variants[a]

ferredoxin I	E_m[b] (mV)	k_{cat} (s^{-1})	K_m (μM)	k_{cat}/K_m (%)[c]
wild-type	−380	139.3 ± 7.2	0.81 ± 0.10	100
htFdI	−370	138.8 ± 8.7	0.78 ± 0.13	103
E15A	−385	123.6 ± 17.7	0.61 ± 0.10	118
D7A/D9A/E10A	−385	128.0 ± 9.4	0.85 ± 0.14	88
Δ62−64[d]	−375	134.8 ± 8.4	0.87 ± 0.15	90
D7A/D9A/E10A/Δ62−64	−370	125.6 ± 9.0	0.65 ± 0.12	112
D7A/D9A/E10A/D28N/E30Q/E32Q	−400	130.4 ± 17.7	0.71 ± 0.12	107
I12T	−360	132.8 ± 8.8	1.23 ± 0.28	63
I12E	−380	104.4 ± 17.4	1.23 ± 0.02	49
I20E	−400	130.4 ± 8.7	0.70 ± 0.13	108
Y35E	−400	150.8 ± 8.9	1.00 ± 0.15	88
D52R	−400	141.7 ± 8.7	1.92 ± 0.28	43
E48A/E49A/D52A	−400	126.7 ± 1.7	1.42 ± 0.29	52
E45A/E46A/E48A/E49A/D52A	−410	113.0 ± 3.7	1.57 ± 0.16	42

[a] Under the assay conditions, FdI and FdI variants couple *Dg* cytochrome c_3 reduction to PFOR oxidation. The rate of Fd reduction in the coupled assay was determined as described in Experimental Procedures. [b] E_m is the redox potential value vs the normal hydrogen electrode. The concentration of FdI and FdI variants used in the measurement of redox potentials by square-wave voltammetry was in the range of 80−150 μM. [c] k_{cat}/K_m values are given as the percentage of the value for wild-type FdI. [d] Δ62−64 is the form in which the EDE tripeptide of the C-terminal extremity has been deleted.

of wild-type FdI, whereas for all the other variants, the K_a is slightly diminished. However, some significant variations of binding enthalpy were observed; as an example, the ΔH value of the D7A/D9A/E10A/D28N/E30Q/E32Q variant ($\Delta H° = 7.3$ kJ/mol) is strongly more favorable than that measured with the D7A/D9A/E10A variant ($\Delta H° = 14.4$ kJ/mol), whereas the free energy is the same ($\Delta G° = -30.2$ and −30.0 kJ/mol, respectively). Thus, it appears clearly that the enthalpy change is counteracted by a favorable entropy change. This enthalpy−entropy compensation is observed for the set of variants studied, and the linear relationship obtained between $\Delta H°$ and $\Delta S°$ provides a slope correlated with the experimental temperature. These results indicate that the variations of enthalpy are probably due to the removal of water molecules from the interacting surface (*27*).

Substitution of Hydrophobic Residues. In addition to the potential role of long-range electrostatic forces in protein−protein interaction associated with charged residues, short-range forces, due mainly to surface hydrophobic residues, make important contributions to the overall binding energy and to the specificity of the interaction between redox partners (*9*, *28*, *29*). Hydrophobic residues I12, I20, and M27 located at the molecular surface surrounding the [4Fe-4S] cluster of FdI as well as Y35 have been substituted with a negatively charged (E) residue. In addition, I12 has been substituted with a polar (T) residue. Among these molecular FdI variants, M27E, I12E, and I12T were unstable. The UV−visible spectrum of the weakly expressed M27E form obtained after the Ni−NTA column was indicative of oxidative damage of the [4Fe-4S] center. Therefore, this highly unstable variant has not been used in the activity assay. The yield of I12E and I12T mutants was only 30% of the amount of htFdI. The midpoint redox potentials of this set of variants (Table 2) are close to that of htFdI except for the redox potentials of I20E and Y35E which are slightly negatively shifted.

All these singly substituted mutants displayed kinetic properties close to those of FdI except I12E and I12T, which showed 51 and 37% decreases in their catalytic efficiency, respectively (Table 2). However, unlike wild-type FdI, I12E and I12T mutants exhibit a $g = 2.01$ [3Fe-4S] cluster EPR signal in the oxidized state, corresponding to approximately 20% of the signal from the reduced protein. The amount of [3Fe-4S] cluster increased over time, which is indicative of the instability of the [4Fe-4S] cluster in these proteins. The instability of I12 variants has not allowed a precise determination of their K_a values. Finally, ITC analysis shows similar effects of I20E and Y35E substitutions as compared to charged residue substitutions (Table 3).

Structural Models of the PFOR−FdI Complex through NMR-Restrained Docking

Two observations can be made from FdI site-directed mutagenesis experiments. (i) No targeted charged residue has a crucial role in complex formation; this result is in disagreement with the high sensitivity of FdI binding affinity to ionic strength as shown by ITC analysis. (ii) Most hydrophobic residues are essential for the stability of the FdI [4Fe-4S] cluster and thus are not good targets for site-directed mutagenesis analysis. Thus, to understand how PFOR and FdI interact, a structural analysis of the complex was carried out through NMR-restrained docking.

NMR Titration of Formation of the PFOR−FdI Complex. The $^{15}N-^{1}H$ HSQC experiment (Figure 3) is the fingerprint of *Da* FdI (at 296 K), where each cross-peak corresponds to the correlation between ^{15}N and ^{1}H atoms of the amide groups. The sequential assignment of these peaks was obtained from heteronuclear NMR experiments. Due to the paramagnetic effect of the FeS cluster at 296 K, only 51 well-resolved correlation peaks were identified among the 64 residues of FdI and used for the mapping of the PFOR interacting site. HSQC experiments have been carried out in the presence of various PFOR concentrations (0.1, 0.2, 0.5, and 1 equiv of FdI). The size of the PFOR dimer (270 kDa) induces line broadening of FdI resonances which increases with PFOR concentration, and most of the lines disappeared at 0.5 equiv. The shifts of the resonances indicate that the complex is in fast exchange at the NMR time scale. Among the 51 resonances observed in the FdI HSQC spectrum (Figure 3), eight resonances (V6, C14, E19, I20, I31, G41, S43, and A50) are notably affected by complex formation (Figure 4A). The mapping of the interacting site of PFOR on FdI revealed an extensive surface area affected by complex formation, including acidic residues largely distributed around the protein.

Docking of the PFOR−FdI Complex. Ab initio docking of the PFOR−FdI complex was generated by BiGGER using PDB entries 1FXR and 1B0P. Figure 5A presents the top 1000 of the initial 5000 hypothetical complexes, ranked according to BiGGER's scoring function. The PFOR dimer is represented here, and a relatively good symmetrical distribution of FdI (each ball represents the FdI center of mass) is observed on the two subunits. Most of the good solutions according to the BiGGER scoring function are located near the distal cluster of PFOR at the potential recognition site suggested by the X-ray structure (*3*).

Table 3: ITC Analysis of *Da* FdI and Molecular Variants Binding to PFOR

ferredoxin I	K_a (M^{-1})	$\Delta G°$ (kJ/mol)	$\Delta H°$ (kJ/mol)	$\Delta S°$ (kJ mol^{-1} K^{-1})
wild-type	$(3.85 \pm 0.38) \times 10^5$	-31.8 ± 0.3	21.3 ± 1.1	0.178 ± 0.004
htFdI	$(4.17 \pm 0.62) \times 10^5$	-32.0 ± 0.4	20.4 ± 1.4	0.176 ± 0.005
E15A	$(4.63 \pm 0.93) \times 10^5$	-32.3 ± 0.5	13.3 ± 0.9	0.153 ± 0.003
D7A/D9A/E10A	$(1.88 \pm 0.19) \times 10^5$	-30.0 ± 0.3	14.4 ± 1.2	0.149 ± 0.004
Δ62−64[a]	$(1.19 \pm 0.18) \times 10^5$	-28.9 ± 0.4	40.1 ± 2.0	0.231 ± 0.007
D7A/D9A/E10A/D28N/E30Q/E32Q	$(1.98 \pm 0.20) \times 10^5$	-30.2 ± 0.2	7.3 ± 0.7	0.126 ± 0.002
I20E	$(1.57 \pm 0.31) \times 10^5$	-29.6 ± 0.5	29.2 ± 1.8	0.197 ± 0.006
Y35E	$(1.04 \pm 0.16) \times 10^5$	-28.6 ± 0.4	45.4 ± 1.8	0.248 ± 0.006
D52R	$(1.19 \pm 0.18) \times 10^5$	-28.9 ± 0.4	32.7 ± 2.0	0.207 ± 0.006
E48A/E49A/D52A	$(1.34 \pm 0.13) \times 10^5$	-29.2 ± 0.3	21.6 ± 1.5	0.170 ± 0.006
E45A/E46A/E48A/E49A/D52A	$(1.04 \pm 0.21) \times 10^5$	-28.6 ± 0.5	31.2 ± 2.2	0.200 ± 0.008

[a] Δ62−64 is the form in which the EDE tripeptide of the C-terminal extremity has been deleted.

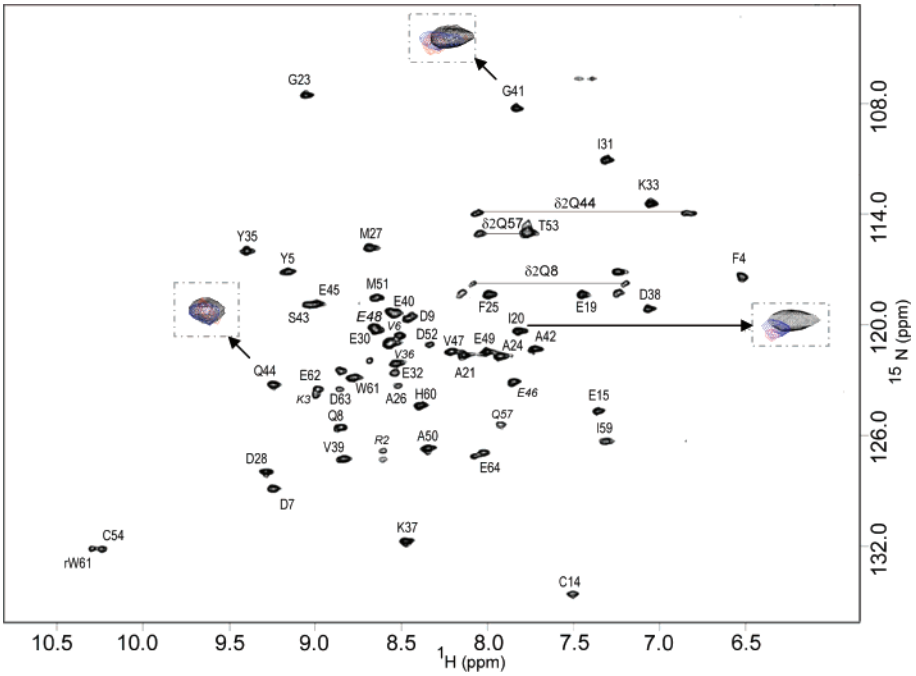

FIGURE 3: $^1H-^{15}N$ HSQC spectrum of *Da* htFdI at 298 K. The FdI concentration was 60 μM, in 20 mM phosphate buffer (pH 6.1). Correlation peaks of amide protons are denoted according to the sequence numbering. The magnified peaks represent cross-peaks for I20, G41, and Q44: black for free FdI, blue for FdI in the presence of PFOR (1:0.1), and red for FdI in the presence of PFOR (1:0.2).

We used the eight residues found to be affected by the interaction in the NMR spectrum to define distance constraints to filter the docking results (Figure 5B). Some docked solutions correspond to the chemical shift variations of the eight residues, but the distances between all the PFOR [4Fe-4S] centers and the FdI [4Fe-4S] center are larger than 20 Å and, thus, correspond to nonphysiological systems. If a distance filter (FeS−FeS distance of <20 Å) is used, the best solutions correspond to poorly NMR-ranked solutions.

This result can be correlated to the large dispersion of the affected residues through the FdI surface and suggests that the PFOR−FdI complex does not exist in a single specific orientation. We have analyzed using Poisson−Boltzmann equation the electrostatic charge distribution of the two proteins. The isopotential representation (Figure 6) shows that the PFOR dimer contains two symmetrical basic depressions (in blue) and that FdI is positively charged around all the molecule (in red), allowing a large number of geometries of the complex if interactions are governed by electrostatics.

To evidence whether the PFOR−FdI complex exists in various orientations, NMR and site-directed mutagenesis experiments were combined to determine some of these geometries. Among the eight affected residues in the NMR spectrum, V6, C14, and I31 are located near the acidic patch of residues (D7, D9, E10, D28, E30, and E32) that have already been mutated. These mutations revealed minor effects on the affinity and the electron transfer within the PFOR−FdI complex (Tables 2 and 3). In contrast, two residues (S43 and A50) are located close to the external side of the FdI large helix which contains many acidic residues not explored through site-directed mutagenesis (Figure 2B). Three new mutants (D52R, E48A/E49A/D52A and the pentamutant, E45A/E46A/E48A/E49A/D52A) corresponding to this patch of acidic residues were generated. Electron transfer measurements (bottom part of Table 2) show that for these three mutants k_{cat} and K_m were slightly affected. The thermodynamic parameters were not different from those of htFdI, but for the pentamutant, K_a was 4 times less than that of the native protein (bottom part of Table 3) and k_{cat} was 42% of the electron transfer efficiency of FdI (bottom part of Table 2). Although not very large, these changes were the largest observed for the different mutants analyzed in this work. Thus, the FdI pentamutant has been used for additional NMR experiments.

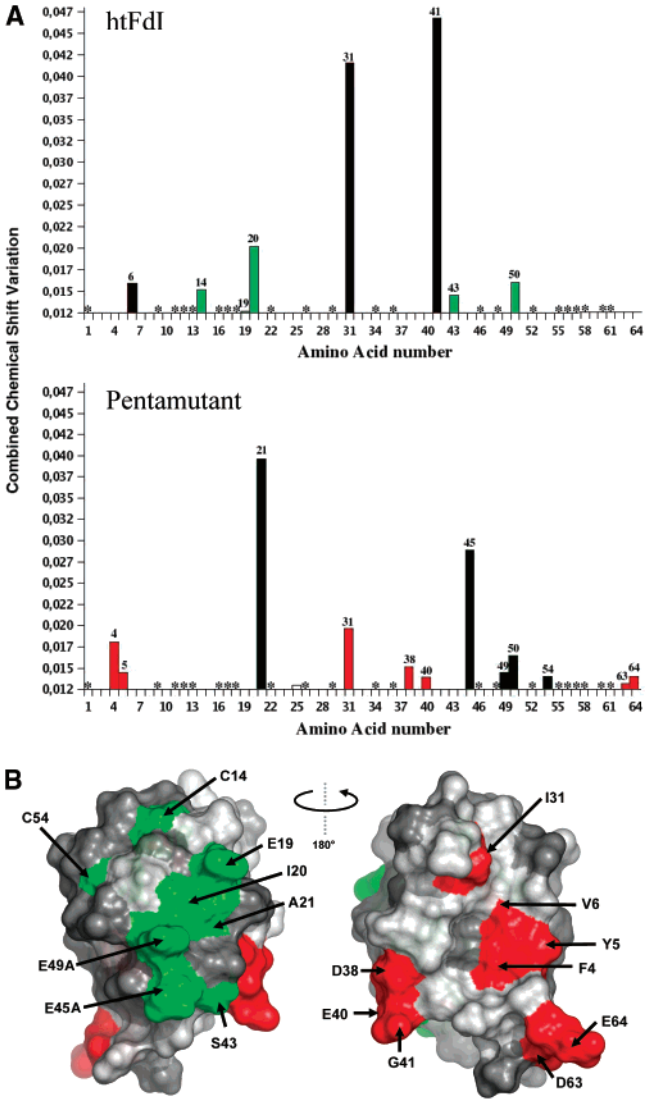

FIGURE 4: (A) Chemical shift variations observed in htFdI HSQC (top) and FdI pentamutant (bottom) in the presence of PFOR (1:0.2). The relative chemical shift variations combine ^{1}H and ^{15}N chemical shifts (*30*). Asterisks denote unassigned residues in FdI HSQC spectra. In the top panel, green sticks indicate residues at site I, and in the bottom panel, red sticks indicate residues at site II. (B) Structural representation of the residues affected in HSQC spectra. In green are the residues located on site I, in the opposite face, and in red the residues located on site II.

NMR Titration of Formation of the Complex between the FdI Pentamutant and PFOR. The HSQC assignments of the FdI pentamutant have been obtained from heteronuclear NMR experiments. HSQC of the pentamutant in the presence of PFOR shows an important line broadening of the resonances, indicating that formation of the complex occurs between PFOR and the pentamutant. However, the affected residues are not identical to those observed with htFdI (Figure 4A). One can observe that residues C14, E19, I20, and S43, perturbed in the FdI spectrum, are not affected in the mutant spectrum, and that two classes of new affected residues are found: F4, Y5, D38, E40, D63, and E64, which correspond to the opposite site of the helix (Figure 4B), and A45, A49, and C54, which are located on the helix (Figure 4B). This indicates that charge neutralization at the FdI helix promotes major changes in the association of Fd with PFOR even if the K_a of the complex is modestly affected. The evolution of residues C14, E19, I20, and S43 in the wild-type protein and of residues F4, Y5, D38, E40, D63, and E64 in the mutant leads us to propose that at least two interacting sites, termed site I (Figure 4B, in green) and site II (Figure 4B, in red), are present on the molecular surface.

Analysis of the Structural Models of the Da PFOR−FdI Complexes. To identify the models corresponding to these two sites among *ab initio* dockings, we used NMR data for htFdI and the pentamutant to filter the solutions, taking into account the possibility that various sites can exist. A model of the pentamutant has been generated, and a new docking calculation has been performed. Figure 7A shows the *ab initio* docking with wild-type (top) and pentamutant (bottom) FdI. The mutations only slightly affect the top 1000 docking solutions.

To select the solutions corresponding to site I and site II, we used two sets of data. In the first case, we used the seven residues (F4, Y5, I31, D38, E40, D63, and E64) affected in the NMR titration with the FdI pentamutant, close to site II (Figure 4B, in red). From the 1000 *ab initio* solutions (Figure 7A), 10 similar solutions were found at an Fe−Fe distance of <17 Å (Figure 7C). Among these 10 solutions, the docking with the best BiGGER score (63/1000) was retained as the "best solution" (Figure 8B). In this model corresponding to site II, FdI faces PFOR at the distal cluster interface with an FeS−FeS distance of 15.59 Å.

In the second case (Figure 7A), we used the residues affected in the htFdI NMR spectra and close to site I (Figure 4B, in green), including residues C14, E19, I20, S43, and A50. Three solutions were found at an FeS−FeS distance of <17 Å (Figure 7C). The three models are very similar, and the solution with the higher BiGGER score (30/1000) was retained as the representative solution for site I (Figure 8A). In this model corresponding to site I, FdI is also in front of the PFOR distal cluster at an FeS−FeS distance of 14.4 Å.

Analysis of the Interacting Surface. Structural models of the PFOR−FdI complex obtained via restrained docking allowed us to propose docking regions on both molecules (Figure 8A,B). The interface between PFOR and FdI in the two models corresponds to an area close to 1500 $Å^2$, in good agreement with the properties of other electron transfer complexes (*31*, *32*). The two complexes are mainly stabilized by salt bridges.

Model of Site I. Electrostatic interactions dominate the complex interface. Residues E19, E45, E46, E48, E49, and D52 located on the external side of the FdI helices are found short distances from lysine residues (K727, K732, K797, K1054, and K1092) of PFOR. With the exception of E19, all these acidic residues were replaced in the pentamutant (E45A/E46A/E48A/E49A/D52A) which is still active in electron transfer with PFOR (Tables 2 and 3). Moreover, the complex is also likely stabilized by salt bridges involving E10, E40, D63, E64, and basic residues of PFOR (K729, K1118, R1100, and K1051, respectively). E10, D63, and D64 were replaced or deleted in the D7A/D9A/E10A/Δ62−64 mutant which is unstable but still active (Table 2). The instability of this mutant strongly suggests that neutralization of all acidic residues involved in site I will prevent production of correctly matured FdI variants.

It should be noted that an additional electrostatic interaction involves a basic residue of FdI (R2) and an acidic residue

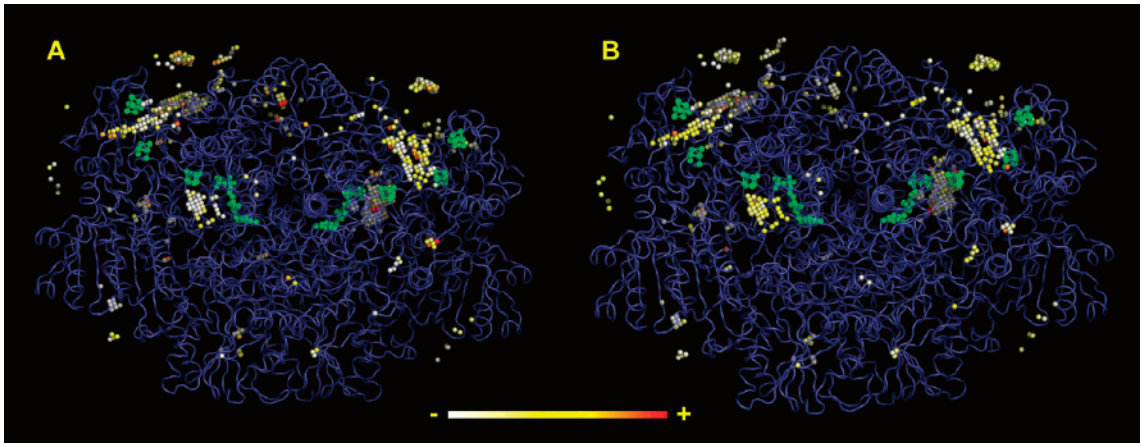

FIGURE 5: Docking of the FdI−PFOR complex. The polypeptide chain of the PFOR dimer is colored blue. Prosthetic groups of the PFOR are colored green. Each ball represents the center of mass of FdI for one of the complexes. (A) The 1000 first *ab initio* docking solutions from BiGGER. The solutions are ranked with the BiGGER scoring function and represented by a colored scale from white to red. (B) NMR scoring of the same solutions. The eight residues of the FdI affected by the presence of PFOR were used to rank *ab initio* models.

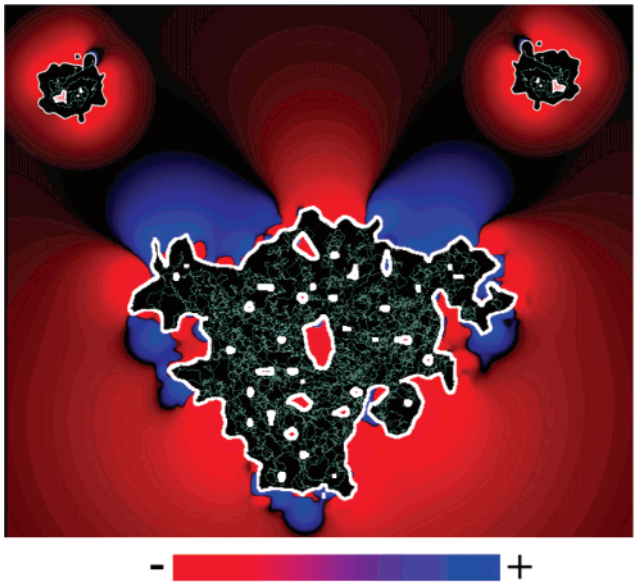

FIGURE 6: Electrostatic charge distribution on the dimer of PFOR (in the center of the figure) and FdI (facing the two depressions of PFOR). The isopotential representation was performed with BiGGER, using the Poisson−Boltzmann equation. Basic charges are represented in blue and acidic residues in red. The PFOR orientation is the same as in Figure 5.

of PFOR (D1116). Moreover, three hydrophobic residues, I12, M51, and W61, are found at the FdI interacting surface.

Model of Site II. The molecular interface also contains a large number of FdI acidic residues (D7, D9, E10, D28, E30, E32, D38, E40, E62, D63, and E64) and lysine or arginine residues of PFOR (K758, K760, K797, K1046, K1051, K1077, K1078, K1082, K1092, R1100, and K1118), indicating that electrostatic interactions are highly involved in this interacting site. Mutation of more than 50% of the carboxylates involved in the site II molecular interface as well as deletion of the C-terminal hook (E62, D63, and E64) led to slight effects on the activity and protein binding (Tables 2 and 3). As observed for the site I model, three hydrophobic residues are found in the site II interface, Y5, I31, and Y35.

Apart from E15, which is found far from these two sites, all the acidic residues of FdI are involved in one of the two interacting sites that we have elucidated and play an essential role in electrostatic interactions. Note that the substitution of E15 affects neither the K_a nor the kinetic parameters of the complex (Tables 2 and 3). Our approach allowed us to reveal two of the geometries of the PFOR−FdI complex. However, additional geometries may exist in solution. Indeed, NMR pentamutant titration shows that neutralization of five charges induced new chemical shift variations compared to the native protein titration (in black in Figure 4A). These mutations highlight other satisfied geometries which are likely to exist in the native complex.

Some common features can be underlined in the models. The FdI interacting site on PFOR is the same in the two models (Figure 7C), located at the highly basic surface surrounding the distal [4Fe-4S] cluster. Six identical basic residues (K797, K1046, K1051, K1092, R1100, and K1118) are found at the interacting surface of the two complexes.

In the two models, C692, one of the distal [4Fe-4S] cluster ligands of PFOR, is close to C54, a ligand of the FdI [4Fe-4S] cluster, suggesting that the two electron transfer sites are very similar. A possible electron pathway can be identified that leads from the distal [4Fe-4S] cluster of PFOR to the [4Fe-4S] cluster of FdI through these cysteine ligands. The close approach of cysteine residues has been previously reported in many redox complexes (*33*, *34*). The C54A FdI mutant was produced but proved to be insufficiently stable for extensive studies even if the new [4Fe-4S] cluster could obtain its fourth ligand from C58, a free cysteine in the native structure (data not shown). In the two sites, the highly conserved I12 residue of FdI is at the interface near the [4Fe-4S] clusters. Substitution of I12 modestly affects the electron transfer reaction between the two proteins but has a marked effect on the stability of the protein.

Reactivity of Da PFOR toward Natural Electron Acceptors

The NMR-restrained docking experiments demonstrated the existence of at least two interacting sites on FdI involving 17 of the 18 acidic residues leading to active configurations of the PFOR−FdI complex. To abolish electron transfer between the two proteins, new mutants targeting all these acidic residues would be required. However, because of the high sensitivity of the [4Fe-4S] Fd to relatively minor structural changes, it may be expected that genes bearing

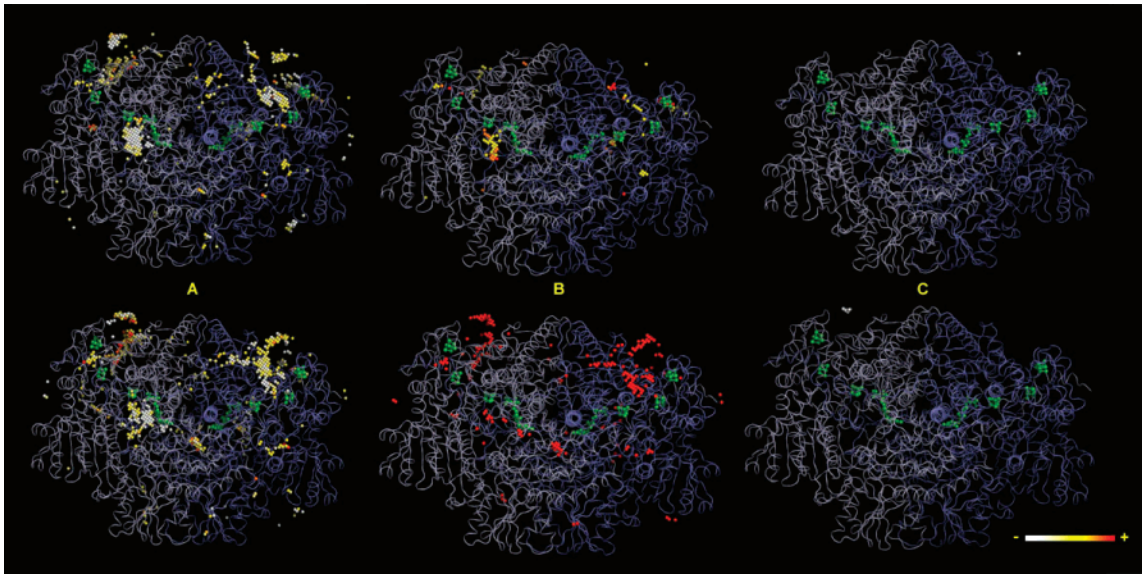

FIGURE 7: Docking of the FdI−PFOR complex with native FdI (top row) and the FdI pentamutant (bottom row). The polypeptide chain of the PFOR dimer is colored blue. Prosthetic groups of PFOR are colored green. Each ball represents the center of mass of FdI for one of the complexes. (A) The 1000 first *ab initio* docking solutions from BiGGER. The solutions are ranked with the BiGGER scoring function and represented by a colored scale from white to red. (B) Solutions filtered by NMR restraints. (C) "Best solutions" using BiGGER's scoring function.

such important modifications failed to give proteins that were sufficiently stable to be produced in *E. coli*. To assess the specificity of the PFOR−FdI system, we used Fds from other closely related species corresponding to natural variants of *Da* FdI. Moreover, various electron carriers without any structural relationship with Fds were also tested, with the aim of identifying the structural and thermodynamic parameters of the redox partner suitable for exchanging an electron with PFOR (Table 4). Our results showed that low-redox potential [4Fe-4S] or 2[4Fe-4S] Fds isolated from *Desulfovibrio* species, *Dmn*, and *Cp* are effective electron carriers of the enzyme. *Da* FdII and *Dmn* FdI contain 14 and 12 conserved carboxylates, respectively, of the 17 acidic residues involved in electrostatic interactions with PFOR and provide at least 95% of the turnover rate (Table 4). This result is in agreement with site-directed mutagenesis on *Da* FdI and demonstrates that D38 which has not been modified is also not crucial for PFOR recognition. *Dg* FdI also contains 12 conserved carboxylate residues and displays 69% of the turnover rate. This decrease in coupling activity may be related to its very low redox potential (Table 4). *Cp* Fd displays a high efficiency (80%) when only six of the 17 acidic residues are conserved. However, *Cp* Fd contains two [4Fe-4S] centers, and the six remaining acidic residues are distributed in their environments: residues 7 and 28 (D9 and E32, respectively, in *Da* FdI) located near cluster I and E18, D34, D36, and D40 (E19, D38, E40, and E46, respectively, in *Da* FdI) around cluster II. In this case, the existence of at least two interacting sites accounts for the high turnover rate with *Da* PFOR.

Dg FdII which supports a very slow electron transfer with PFOR is distinguished from the previously mentioned Fds by its quaternary structure (it is a tetramer), the presence of a [3Fe-4S] cluster of high redox potential, and a structural change corresponding to the rotation of the fourth potential cysteine ligand away from the cluster cavity (*36*). In the same way, rubredoxin, a small acidic protein, exhibiting a high redox potential compared to those of [4Fe-4S] Fds, displays low coupling activity. Among the plant-type Fds tested in the PFOR assay (*37*, *38*), it appears that only *S*sp. Fd which transfers mainly the electrons from PSI to several Fd-dependent enzymes was able to accept electrons from *Da* PFOR with good efficiency. Finally, *Dg* flavodoxin exhibits half the activity of *Da* FdI as the electron carrier in the PFOR assay in keeping with the presence of pyruvate-flavodoxin oxidoreductase activity in some microorganisms (*39*). Moreover, it was previously shown that flavodoxin could substitute for Fd as the electron carrier in pyruvate metabolism by cells of *Cp* grown on media with a low iron concentration (*40*). Conversely, both Fd and flavodoxin are synthesized by some *Desulfovibrio* species (*41*, *42*) grown in media not limited in iron, and flavodoxin was shown to be efficient in replacing Fd in pyruvate oxidation by extracts of *Dg* (*43*). Note that no flavodoxin has been detected in *Da* cells, so far.

DISCUSSION

Pyruvate-ferredoxin oxidoreductase has a crucial role in energy metabolism of anaerobes. In this work, the investigation of the protein−protein redox complex formed by *Da* PFOR and its physiological partner, FdI, has revealed a singular property of this system. The emerging view is that there is no single specific orientation between the protein partners but rather an ensemble of reactive structures governed by electrostatic interactions.

The electron transfer complex exhibits a low binding affinity ($K_a = 3.85 \times 10^5$ M^{-1}) characteristic of transient complex formation (*44*). Moreover, we have shown that K_a is highly sensitive to ionic strength, indicating that electrostatic interactions are essential in formation of the PFOR−FdI complex. Therefore, site-directed mutagenesis of the surface carboxylate residues surrounding the [4Fe-4S] cluster of FdI has been performed in the first part of this work. Surprisingly, the replacement of these residues through many kinds of substitutions shows only a slight effect on the

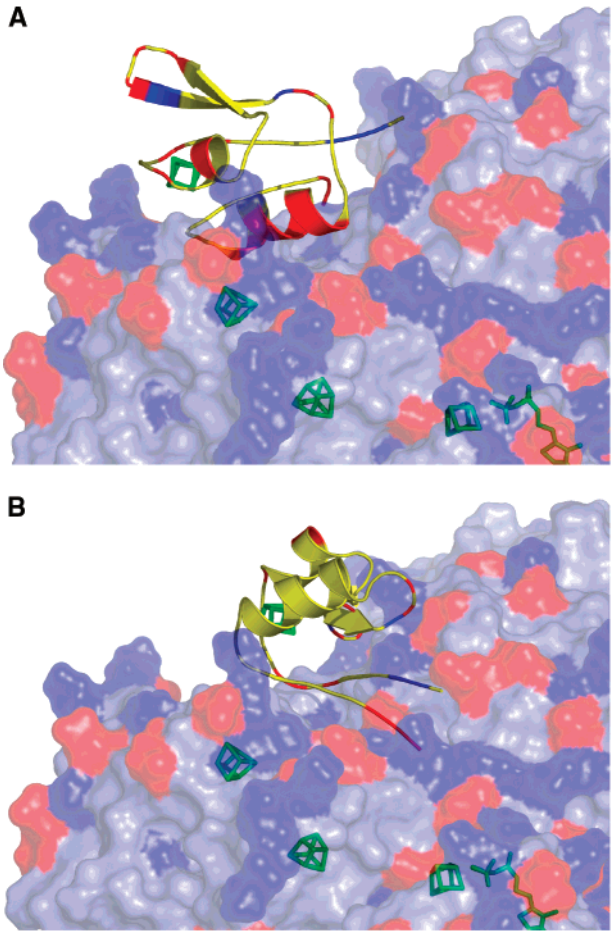

FIGURE 8: PFOR−FdI models from restrained docking. The magnified area of the PFOR interacting site is shown. FdI is colored yellow with a ribbon representation. Basic residues are colored blue and acidic residues red in both molecules. Redox centers of the two molecules are colored green: (A) model of PFOR and native FdI (site I) and (B) model of PFOR and the FdI pentamutant (site II).

Table 4: Reactivity of *Da* PFOR with Natural Electron Carriers[a]

electron carrier[b]	DTE	turnover rate (%)	E_m (mV)[c]
Da FdI	±	100	−385
Da FdII	+	97	−385
Dmn FdI	+	95	−374
Dg FdI	+	69	−455
Dg FdII	−	3	−130
Dmn FdII	+	63	−440, −500
Cp Fd	+	80	−420
Tc Fd	+	40	−400
Ssp. Fd	+	58	−381
Aa Fd1	+	10	−375
Dg Fldx	+	50	−443[d]
Dg Rb	−	10	0

[a] Assays were performed as reported in Experimental Procedures. The activity was determined in the absence of DTE in the assay mixture for the electron carriers which are reduced directly by thiols. Values of the turnover rate are given as the percentage of the value for *Da* FdI. [b] Fldx, flavodoxin; Rb, rubredoxin. [c] E_m is the redox potential value vs the normal hydrogen electrode. [d] Value measured in this work which is in good agreement with that previously obtained for *D. vulgaris* flavodoxin (*35*).

catalytic efficiency and the K_a. Similar results were obtained with 2[4Fe-4S] Fd from *Cp* by assessing the ability of Fd to mediate electron transfer between either PFOR and hydrogenase (*45*) or spinach NADH:ferredoxin oxidoreductase and cytochrome *c* (*46*). In both cases, only minor changes were observed in the activity of Fd variants exhibiting alteration of negatively charged surface residues around cluster II.

These unexpected results of site-directed mutagenesis appeared to be in conflict with the strong dependence of PFOR−FdI binding on ionic strength. Therefore, to gain insight into the nature of the interactions, the structure of the complex was investigated through NMR-restrained docking which is particularly suited to the study of transient redox complexes (*10*, *22*, *23*, *33*). *Ab initio* docking experiments provided evidence that PFOR contains a FdI-interacting site located near the distal FeS cluster. On the other hand, chemical shift perturbation mapping revealed a highly delocalized binding site on FdI, including most of the mutated acidic residues. However, additional residues located at the surface of the large helix region were also present. The neutralization of the five charges at the helix modestly affected the binding affinity and the catalytic efficiency of the PFOR−FdI system. In contrast, the mapping of the interacting surface of this pentamutant, using NMR, was different from that of the native FdI. The combined use of NMR chemical shift mapping, the protein docking program BiGGER, and site-directed mutagenesis experiments provides evidence that the PFOR−FdI complex exists in various reactive configurations rather than in a specific orientation. These various geometries of the complex can be easily illustrated by the isopotential representation of the PFOR and FdI charges (Figure 6). The FdI faces the PFOR at a very basic depression around the distal cluster, and the distribution of acidic charges of FdI allows the protein to assume various orientations. Using the NMR-restrained docking approach, we found two of these geometries among these potential orientations. The analysis of the models indicates that the binding of PFOR with FdI is dominated by electrostatic interactions (10 and 11 acidic residues on FdI for model I and II, respectively), in agreement with the strong dependence of formation of the complex on ionic strength (ref *6* and this work). The models confirm also that most of the mutations carried out on the molecular surface of FdI involve residues located at the interacting surface, in either site I (Figure 8A) or site II (Figure 8B). The neutralization of up to six carboxylate residues at the same time has no dramatic effect on the K_a and the electron transfer activity since charge-dominated binding may still occur with the remaining acidic residues.

The reactivity of PFOR with various bacterial Fds also provided information about the role of conserved acidic residues. The sequence alignment and turnover rate measurements revealed that even if all 17 acidic residues involved in the PFOR−FdI complex are not conserved, homologous Fds provide similar efficiency. From the sequence comparison, only D9 and E40 are common to all these Fds, but are not essential for electron transfer as very different proteins such as plant Fd, flavodoxin, or rubredoxin can react with PFOR, without any conserved residues. In contrast, an essential parameter for the reactivity with PFOR is probably the redox potential of the partner in addition to its acidic property.

Functional information about the hydrophobic and aromatic exposed residues in the vicinity of the FdI [4Fe-4S] cluster is difficult to obtain. Most of the hydrophobic residues

such as M27 are bulky residues involved in the protection of the [4Fe-4S] cluster from the solvent, and the [4Fe-4S] cluster of the M27E variant exhibits high instability (*7*, *47*). Two of the hydrophobic residues (I20 and Y35) were shown not to be crucial in the interaction with PFOR. Note that Y35 is in the model II interface. I12 which is adjacent to the first cysteine ligand of the [4Fe-4S] cluster is found at the electron transfer site in the two models. This residue, highly conserved in Fds (*33*) and in the "Fd-like" domain of various metalloenzymes (*3*, *11*, *48*), was suggested to play an important role in electron transfer reactions (*23*, *33*). In our case, substitutions of I12 (I12E and I12T) were not drastic, demonstrating that it is not essential in the PFOR−FdI system.

Our site-directed mutagenesis results which are in agreement with the lack of a single specific orientation between PFOR and FdI protein partners contrast with observations related to other redox complexes in which interaction between functional partners depends crucially on the presence of specific residues containing either charged or hydrophobic side chains (*49*−*51*). In other respects, formation of the PFOR−FdI complex would consist of an ensemble of orientations involving multiple binding sites, dominated by electrostatics on the contrary of many redox complexes where the interface is largely hydrophobic (*32*, *44*, *52*−*53*). This should allow its flexible mode of binding, ensuring kinetically accelerated productive complex formation and favoring turnover. Previous studies have reported a nonphysiological transient complex between myoglobin and cytochrome b_5 consisting of a dynamic ensemble of structures governed by electrostatics (*54*). The behavior of this redox system appears to display some characteristics common to formation of the PFOR−FdI complex. However, it differs by its lower binding affinity ($K_a \sim 10^4$ M^{-1}).

PFOR exhibits high catalytic activity with various acidic natural electron carriers containing different prosthetic groups (Table 4). Similarly, PFOR from *Pyrococcus furiosus* displayed a high apparent affinity for its own δ subunit coordinating two [4Fe-4S] clusters and homologous to the Fd-like domain of the mesophilic PFOR (*55*). This low specificity can be related to the nature of the PFOR binding site, i.e., a large depression with a great number of basic residues (Figure 6). On the other hand, the existence of multiple binding sites at the FdI molecular surface could be related to the involvement of this low-redox potential electron carrier in various reactions of *Desulfovibrio* energy metabolism, including pyruvate oxidation (*4*, *41*), sulfite reduction (*16*, *56*), and NADPH oxidoreduction (*57*), requiring the interaction of Fd with many physiological redox partners as postulated previously with *Cp* Fd (*46*).

ACKNOWLEDGMENT

We thank Nicole Forget for skillful technical assistance in the purification of proteins and measurements of enzymatic activities. We are grateful to Florence Chaspoul for her invaluable help in microcalorimetric titration experiments and Prof. J.-C. Sari for his advice and suggestions regarding these experiments. We are indebted to Dr. Jean Buc for his expertise in the determination of the kinetic parameters of PFOR and for fruitful discussions throughout this work. We are grateful to Dr. Marie-Hélène Charon for her help in the choice of acidic target residues. We also thank Dr. Marcel Asso and Dr. Bénédicte Burlat for their assistance in EPR spectroscopy measurements. We are indebted to M. Bauzan for growing large-scale cultures of molecular variants. We acknowledge Dr. M.-L. Cardenas for critical reading of the manuscript.

REFERENCES

1. Evans, M. C. W., Buchanan, B. B., and Arnon, D. I. (1966) A new-ferredoxin-dependent carbon reduction cycle in a photosynthetic bacterium, *Proc. Natl. Acad. Sci. U.S.A. 55*, 928−934.
2. Tersteegen, A., Linder, D., Thauer, R. K., and Hedderich, R. (1997) Structures and functions of four anabolic 2-oxoacid oxidoreductases in *Methanobacterium thermoautotrophicum*, *Eur. J. Biochem. 242*, 862−868.
3. Chabrière, E., Charon, M.-H., Volbeda, A., Pieulle, L., Hatchikian, E. C., and Fontecilla-Camps, J.-C. (1999) Crystal structure of pyruvate:ferredoxin oxidoreductase, a central enzyme in anaerobic metabolism, and its complex with pyruvate, *Nat. Struct. Biol. 6*, 182−190.
4. Pieulle, L., Guigliarelli, B., Asso, M., Dole, F., Bernadac, A., and Hatchikian, E. C. (1995) Isolation and characterization of the pyruvate:ferredoxin oxidoreductase from the sulfate-reducing bacterium *Desulfovibrio africanus*, *Biochim. Biophys. Acta 1250*, 49−59.
5. Moser, C. C., Keske, J. M., Farid, R. S., and Dutton, P. L. (1992) Nature of biological electron transfer, *Nature 355*, 796−802.
6. Pieulle, L., Charon, M.-H., Bianco, P., Bonicel, J., Pétillot, Y., and Hatchikian, E. C. (1999) Structural and kinetic studies of the pyruvate:ferredoxin oxidoreductase/ferredoxin complex from *Desulfovibrio africanus*, *Eur. J. Biochem. 264*, 500−508.
7. Sery, A., Housset, D., Serre, L., Bonicel, J., Hatchikian, E. C., Frey, M., and Roth, M. (1994) Crystal structure of the ferredoxin I from *Desulfovibrio africanus* at 2.3 Å resolution, *Biochemistry 33*, 15408−15417.
8. Davy, S. L., Osborne, M. J., and Moore, G. R. (1998) Determination of the structure of oxidised *Desulfovibrio africanus* ferredoxin I by ^{1}H NMR spectroscopy and comparison of its solution structure with its crystal structure, *J. Mol. Biol. 277*, 683−706.
9. Bendall, D. S. (1996) Interprotein electron transfer, in *Protein Electron Transfer* (Bendall, D. S., Ed.) pp 43−68, BIOS Scientific Publishers, Oxford, U.K.
10. Morelli, X., Palma, P. N., Krippahl, L., Guerlesquin, F., and Rigby, A. C. (2001) A novel approach for assessing macromolecular complexes combining soft-docking calculations with NMR data, *Protein Sci. 10*, 2131−2137.
11. Pieulle, L., Magro, V., and Hatchikian, E. C. (1997) Isolation and analysis of the gene encoding the pyruvate:ferredoxin oxidoreductase of *Desulfovibrio africanus*, production of the recombinant enzyme in *Escherichia coli*, and effect of carboxy-terminal deletions on its stability, *J. Bacteriol. 179*, 5684−5692.
12. Nakamura, M., Saeki, K., and Takahashi, Y. (1999) Hyperproduction of recombinant ferredoxins in *Escherichia coli* by coexpression of the ORF1-ORF2-iscS-iscU-iscA-hscB-hscA-fdx-ORF3 gene cluster, *J. Biochem. 126*, 10−18.
13. Hatchikian, E. C., Jones, H. E., and Bruschi, M. (1979) Isolation and characterization of a rubredoxin and two ferredoxins from *Desulfovibrio africanus*, *Biochim. Biophys. Acta 548*, 471−483.
14. LeGall, J., and Forget, N. (1978) Purification of electron-transfer components from sulfate-reducing bacteria, *Methods Enzymol. 53*, 613−634.
15. Papavassiliou, P., and Hatchikian, E. C. (1985) Isolation and characterization of a rubredoxin and a two-(4Fe-4S) ferredoxin from *Thermodesulfobacterium commune*, *Biochim. Biophys. Acta 810*, 1−11.
16. Guerlesquin, F., Bruschi, M., Bovier-Lapierre, G., and Fauque, G. (1980) Comparative studies of two ferredoxins from *Desulfovibrio desulfuricans* Norway, *Biochim. Biophys. Acta 626*, 127−135.
17. Laemmli, U. K. (1970) Cleavage of structural proteins during assembly of the head of bacteriophage T4, *Nature 227*, 680−685.
18. Crestfield, A. M., Moore, S., and Stein, W. H. (1963) The preparation and enzymatic hydrolysis of reduced and S-carboxymethylated proteins, *J. Biol. Chem. 238*, 622−627.

19. Capeillère-Blandin, C., Guerlesquin, F., and Bruschi, M. (1986) Rapid kinetic studies of the electron-exchange reaction between cytochrome c_3 and ferredoxin from *Desulfovibrio desulfuricans* Norway strain and their individual reactions with dithionite, *Biochim. Biophys. Acta 848*, 279−293.
20. Cleland, W. W. (1967) The statistical analysis of enzyme kinetic data, *Adv. Enzymol. 29*, 1−32.
21. Haladjian, J., Thierry-Chef, I., and Bianco, P. (1996) Permselective-membrane pyrolytic graphite electrode for the study of microvolumes of [2Fe-2S] ferredoxin, *Talanta 43*, 1125−1130.
22. Palma, P. N., Krippahl, L., Wampler, J. E., and Moura, J. J. G. (2000) BiGGER: a new (soft) docking algorithm for predicting protein interactions, *Proteins 39*, 372−384.
23. Morelli, X., Dolla, A., Czjzek, M., Palma, N., Blasco, F., Krippahl, L., Moura, J. J. G., and Guerlesquin, F. (2000) Heteronuclear NMR and soft docking: an experimental approach for a structural model of the cytochrome c_{553}-ferredoxin complex, *Biochemistry 39*, 2530−2537.
24. Kauzmann, W. (1959) Some factors in the interpretation of protein denaturation, *Adv. Protein Chem. 14*, 1−63.
25. Hatchikian, E. C., Cammack, R., Patil, D. S., Robinson, A. E., Richards, A. J. M., George, S., and Thomson, A. J. (1984) Spectroscopic characterization of ferredoxin I and II from *Desulfovibrio africanus*, *Biochim. Biophys. Acta 784*, 40−47.
26. Shen, B., Jolie, D. R., Stout, C. D., Diller, T. C., Armstrong, F. A., Gorst, C. M., La Mar, G. N., Stephens, P. J., and Burgess, B. K. (1994) *Azotobacter vinelandii* ferredoxin I. Alteration of individual surface charges and the $[4FE-4S]^{2+/+}$ cluster reduction potential, *J. Biol. Chem. 269*, 8564−8575.
27. Pettigrew, G. W., Goodhew, C. F., Cooper, A., Nutley, M., Jumel, K., and Harding, S. E. (2003) The electron-transfer complexes of cytochrome *c* peroxidase from *Paracoccus denitrificans*, *Biochemistry 42*, 2046−2055.
28. Chothia, C., and Janin, J. (1975) Principles of protein−protein recognition, *Nature 256*, 705−708.
29. Pelletier, H., and Kraut, J. (1992) Crystal structure of a complex between electron-transfer partners, cytochrome *c* peroxidase and cytochrome *c*, *Science 258*, 1748−1755.
30. Garrett, D. S., Seok, Y. J., Peterkofsky, A., Clore, G. M., and Gronenborn, A. M. (1997) Identification by NMR of the binding surface for the histidine-containing phosphocarrier protein HPr on the N-terminal domain of enzyme I of the *Escherichia coli* phosphotransferase system, *Biochemistry 36*, 4393−4398.
31. LoConte, L., Chothia, C., and Janin, J. (1999) The atomic structure of protein−protein recognition sites, *J. Mol. Biol. 285*, 2177−2198.
32. Morales, R., Charon, M.-H., Kachalova, G., Serre, L., Medina, M., Gomez-Moreno, C., and Frey, M. (2000) A redox-dependent interaction between two electron-transfer partners involved in photosynthesis, *EMBO Rep. 1*, 271−276.
33. Morelli, X., Czjzek, M., Hatchikian, E. C., Bornet, O., Fontecilla-Camps, J.-C., Palma, N. P., Moura, J. J. G., and Guerlesquin, F. (2000) Structural model of the Fe-hydrogenase/cytochrome c_{553} complex combining transverse relaxation-optimized spectroscopy experiments and soft docking calculations, *J. Biol. Chem. 275*, 23204−23210.
34. ElAntak, L., Morelli, X., Bornet, O., Hatchikian, E. C., Czjzek, M., Dolla, A., and Guerlesquin, F. (2003) The cytochrome c_3-[Fe]-hydrogenase electron-transfer complex: structural model by NMR restrained docking, *FEBS Lett. 548*, 1−4.
35. Bianco, P., Haladjian, J., Manjaoui, A., and Bruschi, M. (1988) Electrochemical study of flavin mononucleotide and of flavodoxin from *Desulfovibrio vulgaris* Hildenborough, *Electrochim. Acta 33*, 745−752.
36. Kissinger, C. R., Sieker, L. C., Adman, E. T., and Jensen, L. H. (1991) Refined crystal structure of ferredoxin II from *Desulfovibrio gigas* at 1.7 Å, *J. Mol. Biol. 219*, 693−715.
37. Cammack, R., Rao, K. K., and Bargeron, C. P. (1977) Midpoint redox potentials of plant and algal ferredoxins, *Biochem. J. 168*, 205−209.
38. Meyer, J., Clay, M. D., Johnson, M. K., Stubna, A., Münck, E., Higgins, C., and Wittung-Stafshede, P. (2002) A hyperthermophilic plant-type [2Fe-2S] ferredoxin from *Aquifex aeolicus* is stabilized by a disulfide bond, *Biochemistry 41*, 3096−3108.
39. Wahl, R. C., and Orme-Johnson, W. H. (1987) Clostridial pyruvate oxidoreductase and the pyruvate-oxidizing enzyme specific to nitrogen fixation in *Klebsiella pneumoniae* are similar enzymes, *J. Biol. Chem. 262*, 10489−10496.
40. Knight, E., Jr., and Hardy, R. W. F. (1966) Isolation and characteristics of flavodoxin from nitrogen-fixing *Clostridium pasteurianum*, *J. Biol. Chem. 241*, 2752−2756.
41. Akagi, J. M. (1967) Electron carriers for the phosphoroclastic reaction of *Desulfovibrio desulfuricans*, *J. Biol. Chem. 242*, 2478−2483.
42. Dubourdieu, M., and LeGall, J. (1970) Chemical study of two flavodoxins extracted from sulfate reducing bacteria, *Biochem. Biophys. Res. Commun. 38*, 965−972.
43. Hatchikian, E. C., and LeGall, J. (1970) (Study of dicarboxylic acid and pyruvate metabolism in sulfate-reducing bacteria. II. Electron transport; final acceptors), *Ann. Inst. Pasteur 118*, 288−301.
44. Crowley, P. B., Vintonenko, N., Bullerjahn, G. S., and Ubbink, M. (2002) Plastocyanin-cytochrome f interactions: the influence of hydrophobic patch mutations studied by NMR spectroscopy, *Biochemistry 41*, 15698−15705.
45. Moulis, J.-M., and Davasse, V. (1995) Probing the role of electrostatic forces in the interaction of *Clostridium pasteurianum* ferredoxin with its redox partners, *Biochemistry 34*, 16781−16788.
46. Brereton, B. S., Maher, M. J., Tregloan, P. A., and Wedd, A. G. (1999) Investigation of the role of surface residues in the ferredoxin from *Clostridium pasteurianum*, *Biochim. Biophys. Acta 1429*, 307−316.
47. Fukuyama, K., Matsubara, H., Tsukihara, T., and Katsube, Y. (1989) Structure of [4Fe-4S] ferredoxin from *Bacillus thermoproteolyticus* refined at 2.3 Å resolution, *J. Mol. Biol. 210*, 383−398.
48. Nicolet, Y., Piras, C., Legrand, P., Hatchikian, E. C., and Fontecilla-Camps, J.-C. (1999) *Desulfovibrio desulfuricans* iron hydrogenase: the structure shows unusual coordination to an active site Fe binuclear center, *Structure 7*, 13−23.
49. Coghlan, V. M., and Vickery, L. E. (1991) Site-specific mutations in human ferredoxin that affect binding to ferredoxin reductase and cytochrome P450scc, *J. Biol. Chem. 266*, 18606−18612.
50. Hurley, J. K., Fillat, M., Gomez-Moreno, C., and Tollin, G. (1995) Structure−function relationships in the ferredoxin/ferredoxin: $NADP^+$ reductase system from *Anabaena*, *Biochimie 77*, 539−548.
51. Gomez-Moreno, C., Martinez-Julvez, M., Medina, M., Hurley, J. K., and Tollin, G. (1998) Protein−protein interaction in electron-transfer reactions: the ferredoxin/flavodoxin/ferredoxin:$NADP^+$ reductase system from *Anabaena*, *Biochimie 80*, 837−846.
52. Chen, L., Durkey, R., Poliks, B. J., Hanada, K., Chen, Z., Mathews, F. S., Davidson, V. L., Satow, Y., Huizinga, E., Vellieux, F. M. D., and Hol, W. G. (1992) Crystal structure of an electron-transfer complex between methylamine dehydrogenase and amicyanin, *Biochemistry 31*, 4959−4964.
53. Hu, Y., Faham, S., Roy, R., Adams, M. W. W., and Rees, D. C. (1999) Formaldehyde ferredoxin oxidoreductase from *Pyrococcus furiosus*: The 1.85 Å resolution crystal structure and its mechanistic implications, *J. Mol. Biol. 286*, 899−914.
54. Worrall, J. A. R., Liu, Y., Crowley, P. B., Nocek, J. M., Hoffman, B. M., and Ubbink, M. (2002) Myoglobin and cytochrome b_5: A nuclear magnetic resonance study of a highly dynamic protein complex, *Biochemistry 41*, 11721−11730.
55. Menon, A. L., Hendrix, H., Hutchins, A., Verhagen, M. F. J. M., and Adams, M. W. W. (1998) The δ-subunit of pyruvate ferredoxin oxidoreductase from *Pyrococcus furiosus* is a redox-active, iron−sulfur protein: evidence for an ancestral relationship with 8Fe-type ferredoxins, *Biochemistry 37*, 12838−12846.
56. LeGall, J., and Fauque, G. (1988) Dissimilatory reduction of sulfur compounds, in *Biology of Anaerobic Microorg*anisms (Zehnder, A. J. B., Ed.) pp 587−639, John Wiley and Sons, New York.
57. Kremer, D. R., Nienhuis-Kuiper, H. E., Timmer, C. J., and Hansen, T. A. (1989) Catabolism of malate and related dicarboxylic acids in various *Desulfovibrio* strains and the involvement of an oxygen-labile NADPH dehydrogenase, *Arch. Microbiol. 151*, 34−39.

BI0485878